

PAPER • OPEN ACCESS

## Targeting new ways for large-scale, high-speed surface functionalization using direct laser interference patterning in a roll-to-roll process

To cite this article: Christoph Zwahr *et al* 2023 *Int. J. Extrem. Manuf.* **5** 035006

View the [article online](#) for updates and enhancements.

### You may also like

- [Progresses on cryo-tribology: lubrication mechanisms, detection methods and applications](#)  
Wenyan Cui, Hongzhan Chen, Jianxun Zhao *et al.*
- [Advances in 3D printing scaffolds for peripheral nerve and spinal cord injury repair](#)  
Juqing Song, Baiheng Lv, Wencong Chen *et al.*
- [A review of the techniques for the mold manufacturing of micro/nanostructures for precision glass molding](#)  
Tianfeng Zhou, Yupeng He, Tianxing Wang *et al.*

# Targeting new ways for large-scale, high-speed surface functionalization using direct laser interference patterning in a roll-to-roll process

Christoph Zwahr<sup>1,\*</sup> , Nicolas Serey<sup>1</sup>, Lukas Nitschke<sup>1</sup>, Christian Bischoff<sup>2,4</sup>, Ulrich Rädels<sup>2</sup>, Alexandra Meyer<sup>3</sup> , Penghui Zhu<sup>3</sup> and Wilhelm Pfleging<sup>3</sup> 

<sup>1</sup> Laser Precision Manufacturing, Fraunhofer Institute for Material and Beam Technology (IWS), Dresden, Germany

<sup>2</sup> Topag Lasertechnik GmbH, Darmstadt, Germany

<sup>3</sup> Institute for Applied Materials—Applied Materials Physics (IAM-AWP), Karlsruhe Institute of Technology (KIT), Eggenstein-Leopoldshafen, Germany

<sup>4</sup> Institute of Manufacturing Science and Engineering, Technical University Dresden, Dresden, Germany

E-mail: [christoph.zwahr@iws.fraunhofer.de](mailto:christoph.zwahr@iws.fraunhofer.de)

Received 22 December 2022, revised 13 March 2023

Accepted for publication 25 May 2023

Published 19 June 2023



## Abstract

Direct Laser Interference Patterning (DLIP) is used to texture current collector foils in a roll-to-roll process using a high-power picosecond pulsed laser system operating at either fundamental wavelength of 1064 nm or 2nd harmonic of 532 nm. The raw beam having a diameter of 3 mm @  $1/e^2$  is shaped into an elongated top-hat intensity profile using a diffractive so-called FBS®-L element and cylindrical telescopes. The shaped beam is split into its diffraction orders, where the two first orders are parallelized and guided into a galvanometer scanner. The deflected beams inside the scan head are recombined with an F-theta objective on the working position generating the interference pattern. The DLIP spot has a line-like interference pattern with about 15  $\mu\text{m}$  spatial period. Laser fluences of up to 8  $\text{J cm}^{-2}$  were achieved using a maximum pulse energy of 0.6 mJ. Furthermore, an in-house built roll-to-roll machine was developed. Using this setup, aluminum and copper foil of 20  $\mu\text{m}$  and 9  $\mu\text{m}$  thickness, respectively, could be processed. Subsequently to current collector structuring coating of composite electrode material took place. In case of lithium nickel manganese cobalt oxide (NMC 622) cathode deposited onto textured aluminum current collector, an increased specific discharge capacity could be achieved at a  $C$ -rate of 1 °C. For the silicon/graphite anode material deposited onto textured copper current collector, an improved rate capability at all  $C$ -rates between  $C/10$  and 5 °C was achieved. The rate capability was increased up to 100% compared to reference material. At  $C$ -rates between  $C/2$  and 2 °C, the specific discharge capacity was increased to 200  $\text{mAh g}^{-1}$ , while the reference electrodes with untextured current collector foils provided a specific discharge capacity of 100  $\text{mAh g}^{-1}$ , showing the potential of the DLIP technology for cost-effective production of battery cells with increased cycle lifetime.

\* Author to whom any correspondence should be addressed.



Original content from this work may be used under the terms of the [Creative Commons Attribution 4.0 licence](https://creativecommons.org/licenses/by/4.0/). Any further distribution of this work must maintain attribution to the author(s) and the title of the work, journal citation and DOI.

Supplementary material for this article is available [online](#)

Keywords: DLIP, lithium-ion battery, surface texturing, copper, aluminum

## 1. Introduction

The electrification of individual transport is one of the main approaches to decreasing emissions and pollution in the environment and reaching the goal of climate neutrality by the European Union by 2050 [1]. State-of-the-art lithium-ion batteries (LIBs) are already a promising option for stationary and mobile energy storage since high power and energy densities can be realized. However, the current low acceptance of electromobility in society can only be improved by a further significant increase in the electrochemical performance and cost-effectiveness of the energy storage systems used [2]. For this purpose, novel cell designs and specific modifications of active electrodes and inactive materials (separators, current conductors) in LIB production become promising approaches to reaching such goals without additional costly material development.

Among others, texturing electrode components can be a suitable way to increase battery capacity and lifetime [2]. For example, in a study by Pflöging and Pröll [3], homogeneous and drastically accelerated electrolyte wetting was achieved by a laser-based 3D structuring process of two different composite electrode materials (lithium nickel manganese cobalt oxide (NMC) and lithium nickel manganese oxide (LMO)). They showed that microchannels with a width of about 40–55  $\mu\text{m}$  (NMC) and about 70  $\mu\text{m}$  (LMO) and a maximum channel depth indicated the most appropriate wetting behavior. For the NMC material the better electrolyte wetting led to an increase of cell life time (>80% of original discharge capacity) from 141 cycles up to 2290 cycles.

Special interest is also given to the modification of the current collector foils to improve layer adhesion to the active material and thus improve battery lifetime and reduce impedance [4–7]. A good film adhesion is necessary because mechanical failure of the electrode preferentially appears at the phase boundaries between the electrode components due to weak physical interactions and can lead to delamination along the phase boundaries. The physical and electrical connection between the active material particles is destroyed, resulting in a sharp increase in Ohmic resistance due to the electrical interruption between the active material particles. This can be a reason for the electrochemical deterioration of the electrode. The causality between higher surface roughness, increased surface area, and peel strength was demonstrated in different studies using laser and non-laser based approaches [7–9]. Romoli *et al* [7] achieved a 30% higher peel strength using a direct laser writing (DLW) approach on copper utilizing a picosecond pulsed laser source. Zheng *et al* [8] achieved 78% higher tensile strength of a graphite film on an aluminum substrate by using direct laser interference patterning (DLIP) and a picosecond pulsed laser source.

In scaled-up battery production, the coating of composite electrode materials on top of current collector foils is usually established in a roll-to-roll (R2R) process to achieve high processing speed and thus low cost of the final product. The structuring of metallic thin films in a laser-based R2R process was already demonstrated by different groups using a DLW approach to process organic photovoltaics or to achieve antimicrobial or antibacterial properties on stainless steel (SS) ribbons [10, 11]. For the fabrication of laser-induced periodic surface structures (LIPSS) on a SS foil, Mincuzzi *et al* [11] achieved fabrication speeds of up to 5.5  $\text{min m}^{-2}$  using a 500 fs laser and a polygon scanner to deflect the beam on the ribbon.

In terms of laser-based surface processing, DLIP is a relatively novel technique capable of producing surface patterns in various materials in the micro- and sub-micrometer range [12–14]. It offers several advantages over DLW, including higher processing speeds of up to 0.36  $\text{m}^2 \text{min}^{-1}$  (removal rate of 72  $\text{mm}^3 \text{min}^{-1}$ ) for metals and resolutions ranging from 180 nm up to 30  $\mu\text{m}$  [15]. In contrast, DLW is limited in general to structure sizes down to 10–20  $\mu\text{m}$  and removal rates between 2  $\text{mm}^3 \text{min}^{-1}$ –9.5  $\text{mm}^3 \text{min}^{-1}$  [16, 17]. However, by applying DLIP, only repetitive patterns can be fabricated, while DLW can be used to produce highly individualized geometries. The DLIP spot is usually applied as a static ablation tool with a circular-shaped Gaussian intensity distribution, limiting its structure homogeneity. To compensate for this, a high spot overlap and short hatch distance can be used, which reduces the productivity of the process [18]. Additionally, the static DLIP spot requires relative movement of the workpiece using linear stages, further reducing productivity.

To overcome these limitations, several techniques have been developed. For example, Lang *et al* [15] used a DLIP pixel with a line-like elongated geometry and a top-hat intensity distribution to achieve a production speed of 0.36  $\text{m}^2 \text{min}^{-1}$  for metals. However, this configuration requires an incoming rectangular-shaped raw beam geometry that already has a top-hat shape in the long axis, limiting its applicability. El-Khoury *et al* [18] applied top-hat shaping elements into the beam path to achieve a rectangular top-hat DLIP spot from a circular-shaped Gaussian raw beam, resulting in very homogeneous pattern quality. Applying this technique, the process productivity could be increased by about 53% because less overlap is required for texturing. Scanner-based approaches have also been applied for the fabrication of textures on metals, offering advantages over stage-based systems [19, 20]. However, previous approaches were limited to round spot geometries with a Gaussian intensity distribution and low power lasers, which in turn led to limitations in structure homogeneity and a processing speed of about 8  $\text{cm}^2 \text{min}^{-1}$ . Furthermore, scanner-based approaches have only been documented in the literature for non-moving samples, which limits

the size of the area that can be processed, and the achieved scan field width of 72 mm is relatively low [20].

This work presents for the first time DLIP texturing employing beam shaping to produce an elongated, line-like top-hat profile and combines it with a large-area mark-on-the-fly (MOTF) scanner system with a  $120 \times 120 \text{ mm}^2$  processing area, which is powered by a high-power picosecond laser source with 180 W average power. By scanning in the diagonal of the field, combined with a R2R machine, a 170 mm wide structured field is applied to thin metal bands. The pulsed laser system is operating at either the fundamental wavelength of 1064 nm or the 2nd harmonic of 532 nm. The initial round-shaped Gaussian raw beam is shaped into an elongated top-hat intensity profile using diffractive optics and cylindrical telescopes. The line-shaped DLIP spot has a line-like interference pattern with a  $15 \mu\text{m}$  spatial period. Laser fluences of up to  $8 \text{ J cm}^{-2}$  were achieved using a maximum pulse energy of 0.6 mJ. In addition, the in-house built R2R machine is able to handle copper foils with a  $9 \mu\text{m}$  thickness without damaging them. With this equipment, aluminum and copper current collectors with a thickness of  $20 \mu\text{m}$  and  $9 \mu\text{m}$ , respectively, could be processed. Subsequently to current collector structuring and coating of composite electrode material took place. In the case of lithium nickel manganese cobalt oxide (NMC 622) cathode material, an increased specific discharge capacity could be achieved at a  $C$ -rate of 1 C. For the silicon/graphite anode material deposited onto textured copper current collector foils, an improved rate capability at all  $C$ -rates between  $C/10$  and 5 C was achieved ( $C$ -rate  $C/n$ , where  $n$  is the time (h) for complete charge or discharge at the nominal capacity measured at low rates). The rate capability was increased up to 100% compared to reference material with untextured current collector foils. At  $C$ -rates between  $C/2$  and 2 C, the specific discharge capacity was increased to  $200 \text{ mAh g}^{-1}$ , while the reference electrodes showed a specific discharge capacity of  $100 \text{ mAh g}^{-1}$ , showing the potential of the DLIP technology for cost-effective production of battery cells with increased cycle lifetime.

## 2. Methods and materials

As current collectors, aluminum foils with  $20 \mu\text{m}$  thickness and copper foils with  $9 \mu\text{m}$  thickness were used. The copper foils were purchased from MTI Corporation (KJ group) (material copper, purity  $>99.8\%$ ) and aluminum foils from AlFiPa (material aluminum  $>99.0\%$  EN-AW 1200 Norm).

### 2.1. DLIP

The periodic patterns are generated using a pulsed Nd:YVO<sub>4</sub> solid-state laser system (PX400–2–GF, Edgewave GmbH, Germany) with a fundamental wavelength of 1064 nm, a pulse duration of 10 ps, a pulse repetition rate of 250 kHz, and 0.88 mJ pulse energy for a maximal power of 220 W. The beam path used for DLIP processing is shown in figure 1. The recently developed approach uses two interfering line spots with an adjustable high aspect ratio, which were generated using an especially designed 1D beam shaper and two

crossed cylindrical telescopes. In the working plane, the two partial line spots have a homogeneous top-hat energy distribution along the major axis and a Gaussian distribution along the minor axis. The optical setup is described in detail in the following paragraphs:

The raw beam having a diameter of 3 mm @  $1/e^2$  is first shaped by the novel FBS<sup>®</sup>-L element (TOPAG GmbH, Germany), which is based on the so-called Fundamental Beam Shaping (FBS<sup>®</sup>) concept [21] and described in detail later. Two separate optical telescopes consisting of cylindrical lenses were placed behind the FBS<sup>®</sup>-L beam shaping element. The first two cylindrical lenses (the top-hat telescope) reduce the beam size by a factor of 2 and have their cylindrical axes perpendicular to the top-hat direction. The second cylindrical telescope (Gaussian telescope) uses the same cylindrical lenses, but in reverse order to expand the beam by a factor of two and with the cylindrical axis aligned parallel to the top-hat profile. By varying the lens distance of each telescope, a divergence of the two independently controlled axes can be introduced. The significance of this feature is described in more detail in the next paragraphs, as it allows precise control of the DLIP pixel. The shaped beam is split by a diffractive optical element (DOE) into its diffraction orders, where about 79% of the power is equally distributed to the two first diffraction orders. The first diffraction orders are paralyzed using a prism and guided into a galvano-scanner (Racoon21, Novanta Photonics, Wackersdorf, Germany). Finally, the deflected beams inside the scan head are recombined with an F-theta objective with a 191.4 mm focal length on the working position (S4LFT0192/126, Sill Optics GmbH, Germany), generating the interference pattern (DLIP pixel).

The interference of the two laser beams at the focal plane caused a line-like intensity modulation, which is given by equation (1):

$$\Phi(x, y) = 4\Phi_0 \cos^2\left(kx \sin \frac{\alpha}{2}\right) \quad (1)$$

where  $\Phi_0$  is the laser fluence of each beam,  $\alpha$  is the angle of incidence between the interfering beams, and  $k = 2\pi\lambda^{-1}$  is the wave number at the laser wavelength  $\lambda$ . The half intersection angle between the beams  $\alpha$  defines the spatial period  $\Lambda$  between two intensity maxima of the structure, which is given by equation (2):

$$\Lambda = \frac{\lambda}{2 \sin \alpha} \quad (2)$$

**2.1.1. FBS<sup>®</sup> concept.** The FBS<sup>®</sup> concept allows the generation of several two-dimensional top-hat profiles and is used in different applications [18, 22–24]. Thus, it is possible to create five different top-hat profiles with a square footprint along the caustic of a focused beam. There are two profiles in front (–2nd, –1st order), two profiles behind (+1st, +2nd order), and one profile in the focal plane (zero order) of a focusing lens. The position and size of the  $\pm 2$  and  $\pm 1$  orders depend on the position of the beam shaper in the beam path and the numerical aperture of the focused beam [25, 26]. In

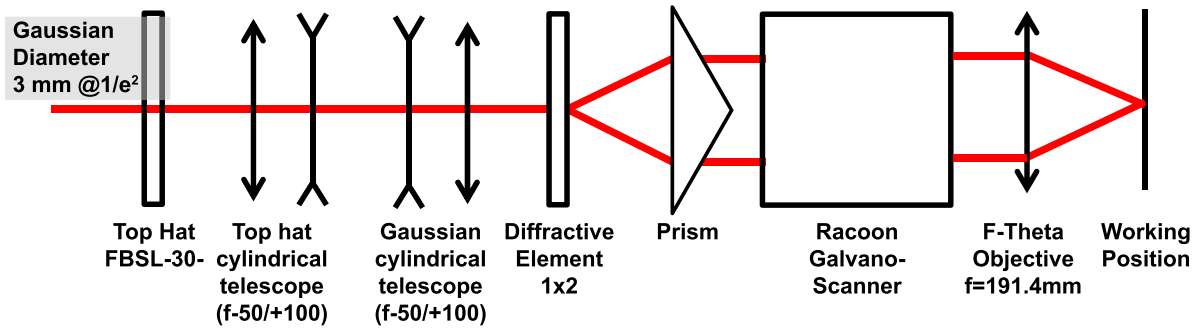


**Figure 1.** Illustration representing the optical path of the laser beam with 1064 nm wavelength. The raw beam diameter is 3 mm@1/e<sup>2</sup> and shaped to an elongated interference pattern having a top-hat distribution along the major axis.

combination with a cylindrical telescope, one axis of the beam can be changed in size, resulting in a different numerical aperture for one axis of the focus and thus a top-hat rectangular profile in the focal plane. A non-ideal collimation behind the cylindrical telescope makes it possible to generate additional refractive power for this axis and to vary the position of the individual orders along the caustic. This allows shaped profiles of the separated axes to be combined [26].

The novel beam shaping type FBS<sup>®</sup>-L used in this work enables 1D beam manipulation and allows the generation of a top-hat intensity distribution along one axis in the focal plane, while maintaining the original Gaussian beam profile on the other axis, similar to [27–29]. The investigations in this work have shown that even in the case of the one-dimensional FBS<sup>®</sup>-L beam shaping, there are five different 1D top-hat profiles along the caustic of the shaped axis. This behavior is comparable to the 2D case described in the previous paragraph.

**2.1.2. Simulations.** For the simulation of the optical performance, the commercial physical optics software VirtualLab Fusion was used, on a workstation with an AMD Ryzen™ Threadripper™ 2990WX processor, 32 cores, 3 GHz and 128 GB RAM memory.

For a better understanding of the propagation behavior of the FBS<sup>®</sup>-L-shaped beam, a simple optical setup was used. A Gaussian laser beam with a wavelength of 1064 nm, an input beam diameter of 1.5 mm @ 1/e<sup>2</sup> is focused by a lens with a focal length of 191.4 mm. The FBS<sup>®</sup>-L beam shaper is placed 200 mm in front of the lens. First of all, the beam shaper in the beam path was omitted in order to see the behavior of the Gaussian beam. Figure 2 shows the caustic in the area of the focal plane for a focused Gaussian laser beam without FBS<sup>®</sup>-L in the beam path.

To generate this image, several cross-sections of the intensity profile along the *x*-axis (*y* = 0) are calculated at different positions along the propagation axis *z* (optical axis) and strunged together. The displayed image is normalized to the maximum intensity. This procedure is also used for further illustrations of a caustic.

By placing the FBS<sup>®</sup>-L element for the *x*-axis 200 mm in front of the focusing optics, the caustic is changed according to figure 3(a) (green axes). The position of the beam shaper

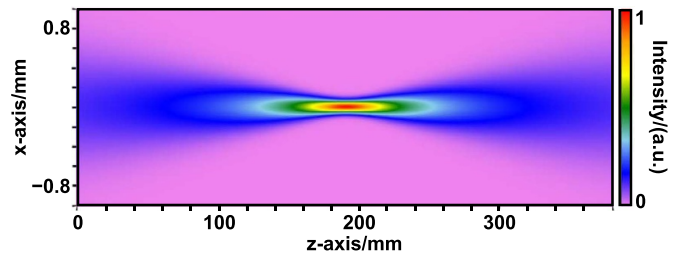


**Figure 2.** Caustic of focused Gaussian beam, input beam diameter 1.5 mm@1/e<sup>2</sup>, focal length 191.4 mm, same caustic for *x*- and *y*-axes.

was selected in such a way that the caustic shows a symmetrical propagation behavior with respect to the focal plane. This is because the position of the individual beam shaper in the optical system and the numerical aperture of the focused beam have an influence on the symmetry properties of the caustic [26]. Nothing changes for the *y*-axis, so it still corresponds to figure 2.

A closer look at the symmetrical caustic of figure 3(a) reveals five top-hat profiles at various *z*-positions, which are indicated. The normalized cross-sections of the top-hat profiles ±2TH (second order), ±1TH (first order) and *z*TH (zero order) are shown in figures 3(b)–(e). In the case of a symmetric caustic, the profiles of an order are nearly identical in shape and size.

If the crossed cylindrical telescopes described above are introduced into the beam path, between the FBS<sup>®</sup>-L element and the focusing lenses, the beam gets elliptical. If the diameter of the Gaussian beam in front of the telescopes is 3 mm@1/e<sup>2</sup>, the unshaped *y*-axis behind the telescopes has a Gaussian intensity distribution with a major axis of 6 mm@1/e<sup>2</sup>. The *x*-axis still has a diameter of 1.5 mm, but due to the diffractive beam shaping, the intensity distribution shows a strong modulation.

The concept of the crossed cylindrical telescopes has the advantage that the focused *y*-axis shows a larger numerical aperture and thus a narrower line width in the working plane, which increases the fluence. In addition, the spot width of the Gaussian profile at the working plane can be controlled by changing the divergency of the second telescope (Gaussian telescope). On the other hand, the length and

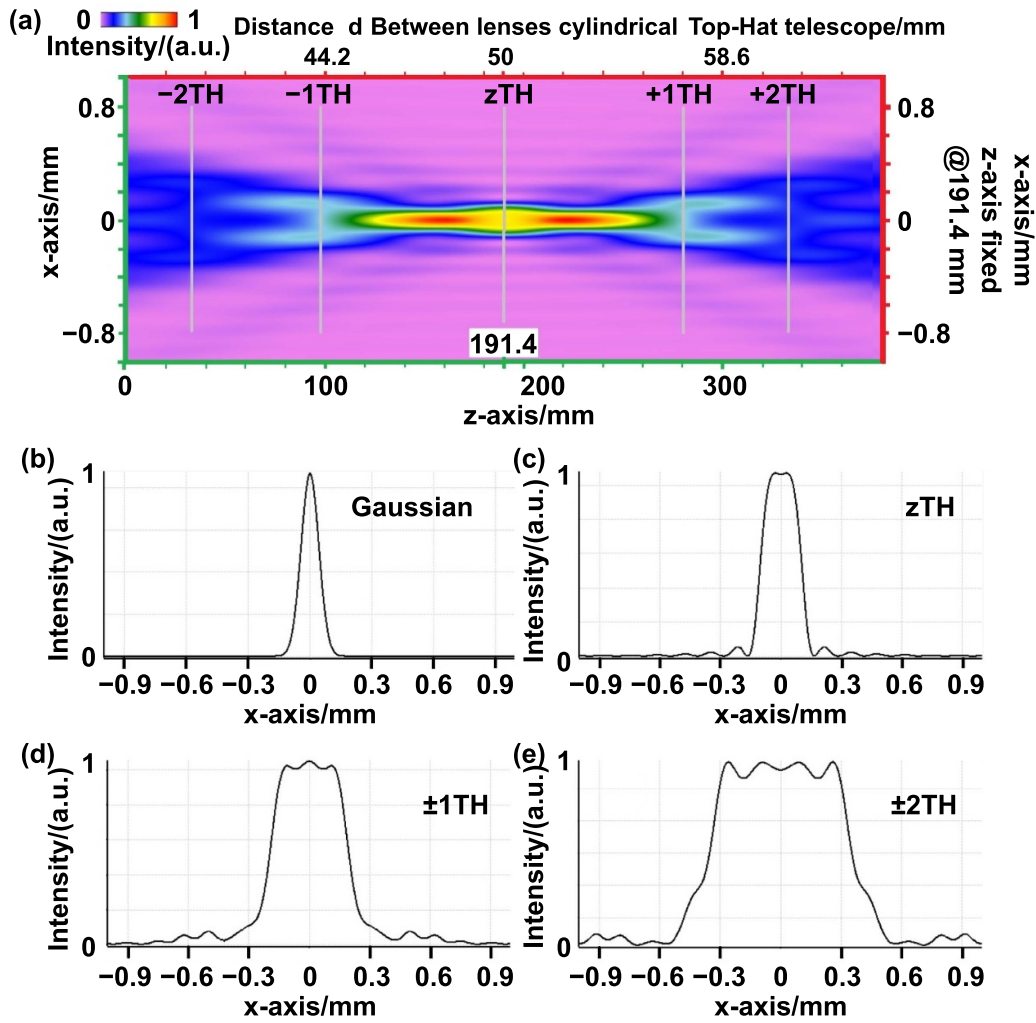


**Figure 3.** Caustic profiles at various  $z$ -positions. (a) Caustic of FBS<sup>®</sup>-L shaped focused beam ( $x$ -axis), input beam diameter 1.5 mm@ $1/e^2$ , focal length 191.4 mm, (b)–(e) show different cross-sections: For an unshaped Gaussian beam at the focal plane (b), a zero-order top-hat zTH at the focal plane (c), first-order top-hats  $\pm 1TH$  (d), and second-order top-hats  $\pm 2TH$  (e), each graph is normalized individually.

intensity distribution of the  $x$ -axis in the working plane can also be influenced. By modifying the distance  $d$  between the lenses of the first cylindrical telescope (top-hat telescope), the beam divergence can also be adjusted. This allows the caustics of the  $x$ -axis to be shifted along the  $z$ -axis, and thus the plane of the desired top-hat profile can be placed in the working plane defined by the Gaussian  $y$ -axis. As a result, the line aspect ratio and the laser fluence on the sample can be easily controlled.

This principle is illustrated in figure 3(a) (red axes). If the distance  $d$  of the lenses of the first telescope (top-hat telescope) is changed, the cross-section in the focal plane of the focusing lens at  $z = 191.4$  mm is also changed. When the distance  $d$  between the telescope lenses is 50 mm the telescope delivers a collimated beam, and in the focal plane of the focusing lens, the zero-order top (zTH) can be seen. By varying the distance  $d$  between the telescope lenses to a value less than or greater than 50 mm, the other top hat profiles,  $\pm 2TH$  and  $\pm 1TH$ , can be placed in the focal plane. In principle, the top-hat profiles  $\pm 2TH$ ,  $\pm 1TH$  and zTH show the same intensity distributions as shown in figures 3(b)–(e). There are only minor changes

in the length and shape of the top-hat profiles compared to figures 3(b)–(e). At the same time, the Gaussian telescope is set to ideal collimation so that the perpendicular Gaussian  $y$ -axis always has the narrowest line width for all cross-sections shown.

Finally, the optical setup in the simulation was expanded to include the essential DLIP components, the DOE for beam splitting and the prism for parallelization of the two sub-beams. It should be noted that the distance of the DOE prism determines the distance of the parallel partial beams behind the prism. And thus, according to equation (2), it influences the spatial period  $\Lambda$  of the DLIP pixel. The resulting interference effects in the area of the focal plane, taking into account all relevant parameters of the experimental setup, are shown in figure 4.

Figures 4(a)–(c) show the interference effects without a beam shaper and a distance  $d = 50$  mm for the first cylindrical telescope. Figure 4(a) shows the crossing point of the two Gaussian beams. The so-called interference volume is clearly visible. In addition, a slight variation of the spatial

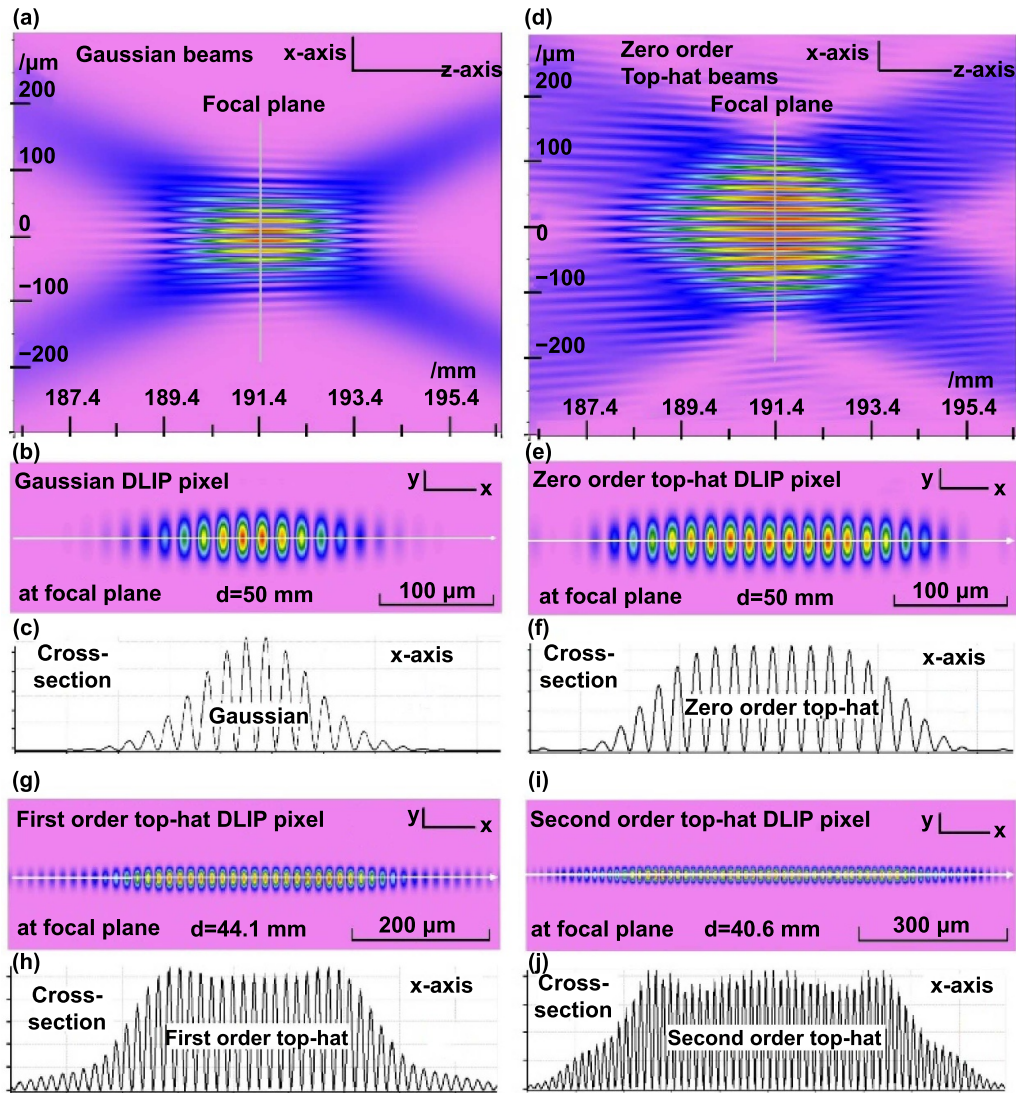


**Figure 4.** Interference effects in the area of the focal plane, (a) crossing point of two Gaussian beams, (b) Gaussian DLIP pixel, (c) cross-section of Gaussian DLIP pixel, (d) crossing point of two zero order top-hats, (e) zero order top-hat DLIP pixel, (f) cross-section of zero order top-hat DLIP pixel, (g) first order top-hat DLIP pixel, (h) cross-section of first order top-hat DLIP pixel, (i) second order top-hat DLIP pixel, (j) cross-section of second order top-hat DLIP pixel.

period for different  $z$  positions can be seen. This variation is in the range of  $2.5\% \text{ mm}^{-1}$  with respect to the spatial period in the focal plane. The resulting DLIP pixel in the focal plane at  $z = 191.4 \text{ mm}$  with a spatial period  $\Lambda$  of  $15.3 \mu\text{m}$  is shown in figure 4(b). The associated intensity curve along the  $x$ -axis can be seen in figure 4(c). The enveloping Gaussian profile is clearly visible.

Figures 4(d)–(f) show the interference effects with the FBS<sup>®</sup>-L in the beam path and a distance  $d = 50 \text{ mm}$  for the first cylindrical telescope. Figure 4(d) shows the crossing point of the resulting zero order top-hat profiles. A slightly bigger interference volume is visible, with a more homogeneous distribution along the  $x$ -axis. Figure 4(e) shows the resulting DLIP pixel for the zero-order top hat in the focal plane at  $z = 191.4 \text{ mm}$ . The spatial period  $\Lambda$  is not affected by the use of the beam shaping element and is still  $15.3 \mu\text{m}$ . The associated

intensity curve along the  $x$ -axis can be seen in figure 4(f). Also, the relative variation of the spatial period for different  $z$ -positions is in the range of  $2.5\% \text{ mm}^{-1}$ .

By changing the distance  $d$  of the top-hat telescope, the geometry of the pixel can be changed as described above. For the distance  $d = 44.1 \text{ mm}$ , the first-order top-hat can be placed in the focal plane, and the DLIP pixel shown in figure 4(g) results. The cross-section shows very good homogeneity over a significantly longer section (figure 4(h)). If the distance  $d$  of the top-hat telescope is  $40.6 \text{ mm}$ , the second-order top-hat can be placed in the focal plane. This allows the length of the DLIP pixel to be further increased, as shown in figure 4(i). At the same time, homogeneity is preserved (figure 4(j)). The higher-order top-hat profiles also have no significant influence on the spatial period  $\Lambda$  or the relative variation of the spatial period for different  $z$ -positions.

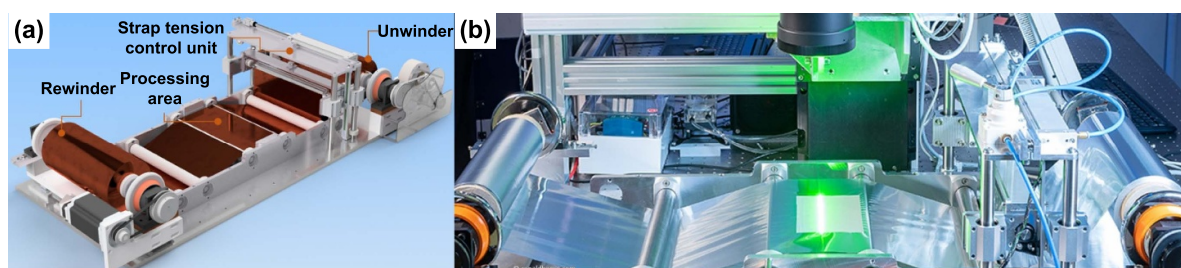


**Figure 5.** Display of roll-to-roll setup. (a) Detailed picture of the roll-to-roll CAD model illustrating the main parts of the in-house built roll-to-roll machine. (b) Image of the machine processing aluminum foil using a laser beam with a wavelength of 532 nm.

## 2.2. R2R processing

The R2R machine to wind up the foils is an in-house build solution (Fraunhofer IWS, Dresden, Germany) and is shown in figure 5. It offers a web width of up to 300 mm and a maximum web speed of up to  $10 \text{ m min}^{-1}$ . It mainly consists of an unwinder, a strap tension control unit, the laser processing area stretched by two rollers, and the rewinder to move metallic foils. It also has a long travel of the tensioning roller and a magnetic powder brake, so that vibrations and wrinkling can be reduced during the process and the accuracy of the web speed can be increased. The system also has an additional encoder to use the MOTF function of the Novanta scanner.

## 2.3. Electrochemical and mechanical characterization

In order to study the effect of current collectors with different DLIP patterns on the electrochemical properties of composite electrodes,  $\text{Li}(\text{Ni}_{0.6}\text{Mn}_{0.2}\text{Co}_{0.2})\text{O}_2$  (NMC622, from BASF SE, Germany) and Si/graphite (silicon: nanomakers, France; graphite: SGPT808, Targray, Canada) coating recipes were developed at KIT and applied for the manufacturing of cathodes and anodes, respectively.

For cathode manufacturing, polyvinylidene fluoride (PVDF) Solef 5130 (Solvay Specialty Polymers, France) was used as a binder, while carbon black C-ENERGY Super C65 (Imerys G&C, Belgium) and KS6L Graphite (Imerys G&C, Switzerland) were applied as conductive agents. The mixing procedure as well as the composition of the cathode slurry were described in detail elsewhere [30]. Afterwards, the slurry was tape casted onto the patterned aluminum foil with  $20 \mu\text{m}$  thickness on a laboratory coater (MSK-AFA-L800-LD, MTI Corporation, USA) and dried at  $90 \text{ }^\circ\text{C}$  for 2 h. Then the cathode film was calendered by a rolling presser (MSK-2150, MTI Corporation, USA) to achieve a 35% porosity. The cathodes were stored in a vacuum oven at  $130 \text{ }^\circ\text{C}$  for 16 h prior to assembly in coin cells.

Silicon/graphite anodes were prepared via ball milling. Commercially available silicon nanopowder (nanomakers, France) and graphite (SGPT808, Targray, Canada) were used as active materials. As binder, sodium carboxymethyl cellulose (CMC, MTI Corporation, Richmond, CA, USA) and styrene butadiene rubber (SBR, 50% solid content, MTI Corporation, Richmond, CA, USA) were applied. Carbon black (CB, C-nergy Super C65, Imerys G&C, Paris, France) was used as a conductive agent. The mixing procedure and the

composition of the anode slurry were described elsewhere [31]. The slurry was tape casted on the patterned copper current collector on a laboratory coater (MSK-AFA-L800-LD, MTI Corporation, USA) with a doctor blade distance of  $150 \mu\text{m}$ . The drying was performed at ambient temperatures. The anodes were subsequently calendered by a rolling presser (MSK-2150, MTI Corporation, USA) to reach a porosity of 40%.

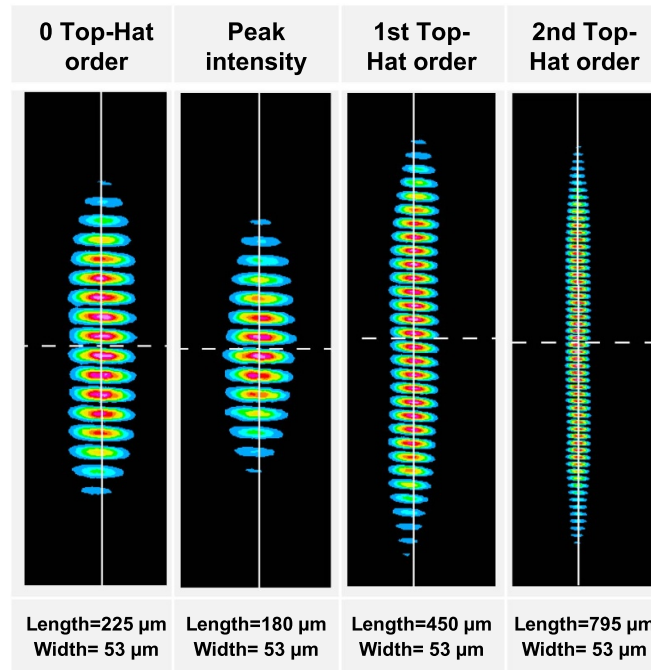
Cell assembly has been illustrated elsewhere [31, 32]. The rate capability test was carried out using a battery cycler (BT2000, Arbin Instruments, USA). The constant current-constant voltage method was applied during charging/discharging processes for cells with NMC 622 or Si/graphite versus lithium, i.e. in half-cell setup. The first 3 cycles were performed at  $C/20$  (one additional  $C/50$  cycle for Si/graphite anodes) as the formation step. Afterwards, the  $C$ -rates increased from  $C/10$  to 5 C ( $C/10$ ,  $C/5$  with 5 cycles each;  $C/2$ , 1 C, 2C, 3 C and 5 C with 10 cycles each). The lower and upper cut-off voltages of cells containing NMC 622 were 3.0 and 4.3 V, respectively. For Si/graphite electrodes, the voltage window was 0.06–1.2 V. For each electrode modification, a minimum of three cells were assembled.

A static materials testing machine (Zwick Roell Group, Germany) was applied to conduct a  $90^\circ$ -peel-off test in order to measure the film adhesion of electrodes with different DLIP-patterned current collectors. The electrodes were cut in  $1.7 \times 8 \text{ cm}^2$  strips. During the peeling test, a constant peeling speed of  $10 \text{ mm s}^{-1}$  was set while the load was recorded. After the measurement, the average force needed to peel off the electrode material from the current collector was calculated, and the adhesion strength is defined as the mean force divided by the sample width, which was kept constant at 1.7 cm for all samples.

## 3. Results and discussion

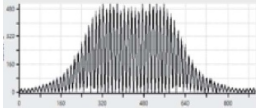
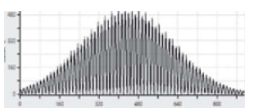
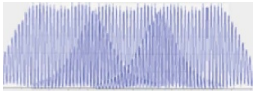
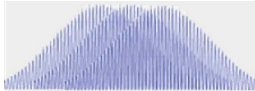
### 3.1. Surface texturing using a line top-hat beam shaping element

A beam shaping element type FBS<sup>®</sup>-L from TOPAG is used in the beam path to achieve a 1D beam manipulation in which a top-hat is generated on the major axis while the original beam profile (Gaussian) is maintained on the minor axis. In the working position, the two sub-beams exhibit a top-hat energy distribution along the major axis and a Gaussian distribution



**Figure 6.** Beam profile camera images of the DLIP pixels with different top-hat orders of the FBS<sup>®</sup>-L optical element produced by superimposing two partial beams on the substrate.

**Table 1.** Comparison of achievable processing speeds and useable pulse energies using top-hat and Gaussian energy distributions at the major axis of the elongated interference pixel.

	Top-hat	Gauss
Beam profile		
Laser frequency		250 kHz
Hatch distance	390 μm	150 μm
Scanning speed		18.75 m s <sup>-1</sup>
Processing speed	0.39 m <sup>2</sup> min <sup>-1</sup>	0.15 m <sup>2</sup> min <sup>-1</sup>
Band speed	2.6 m min <sup>-1</sup>	1.0 m min <sup>-1</sup>
Fluence		3.48 J cm <sup>-2</sup>
Pulse energy	0.90 mJ	0.39 mJ
Peak matching		

along the minor axis. With the optical setup shown in figure 1, it is possible to control the aspect ratio of the DLIP pixel and the laser fluence on the sample. The shape of the DLIP pixels for different top-hat orders was measured using a beam profile camera. Figure 6 shows the beam profiles that can be realized by the FBS<sup>®</sup>-L element in combination with the direct laser interference method at 1064 nm. Different orders (orders: 0, 1, 2) are shown as examples at which an optimally pronounced intensity distribution can be realized. The controlled adjustment of the two-cylinder telescopes makes it possible to generate beam profiles with a length of 180 μm–795 μm (major axis) and a defined width of 53 μm (minor axis). The measured line widths and line lengths differ only slightly from the simulation data. The line length deviation is less than 10%.

The width of the lines has a deviation of about 25%, which can be explained by the beam quality  $M^2$  of the laser.

The use of the top-hat profile has certain advantages regarding achievable processing speeds and the useable pulse energy of the laser system. In table 1, the first top-hat order is compared with the Gaussian-shaped line-like spot that can be achieved without the FBS<sup>®</sup>-L element. For the calculation of the possible processing speed, the laser frequency and cumulative laser fluence on the surface are kept constant. On the foil, the line-like structures are oriented perpendicular to the moving direction of the R2R machine. Because of the higher peak energy of the Gaussian beam, the lines cannot be separated by more than about one-third of the beam diameter without producing a sinusoidal variation in depth perpendicular to the

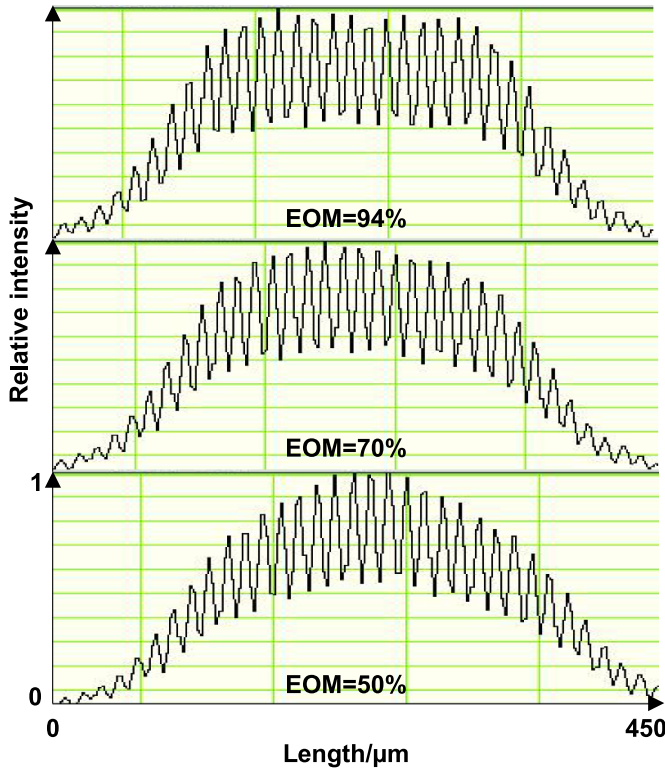


**Figure 7.** Measured evolution of the top-hat profile for different power sets of the electro-optic modulator (EOM) of the laser system.

process direction. On the other hand, the top-hat profile produces a homogeneous depth over a larger width, and the ends of the beam can be superimposed until the cumulative fluence reaches the top-hat level. In consequence, the hatch distance for the top-hat profile is  $390 \mu\text{m}$  while for the Gaussian profile, the hatch distance needs to be  $150 \mu\text{m}$  to achieve homogeneous peak matching. Therefore, the scanning speed using the Gaussian profile is only 38% of the top-hat profile, and consequently, the processing using the top-hat profile can be 2.6 times faster. Furthermore, using the Gaussian profile, the full pulse energy of the laser system cannot be used, as the number of pulses needed to reach the cumulated fluence of  $3.48 \text{ J cm}^{-2}$  is also 2.6 times greater than for the top-hat shape.

Measuring the profile of the first top-hat order with varying laser powers, it was found that the beam caustic changed. Changing the pulse energy or repetition frequency shifted the position of the top-hat profile in the beam path out of the DLIP interference volume. The measured top-hat profiles for 50%, 70% and 94% power set of the electro-optic modulator are shown in figure 7. Despite this challenge in setting up the beam path, the process windows that can be realized are considered sufficiently large and thus suitable for microtexturing with the DLIP process. Moreover, the collimation of the first cylindrical telescope (figure 1) can be adjusted to the top-hat profile to be generated, so that the position of the top-hat beam profile can be optimized with respect to the target working position.

The FBS<sup>®</sup>-L element using the 1st top-hat order was tested experimentally on an aluminum sample with the maximum available power of the laser system (at the second harmonic

wavelength  $\lambda = 532 \text{ nm}$ ; repetition rate: 250 kHz; pulse energy: 0.66 mJ) and constant scanning speed ( $500 \text{ mm s}^{-1}$ ). The focal length of the f-theta objective was 292 mm, and the setup was adjusted to achieve a spatial period similar to that at the 1064 nm wavelength. The hatch distance was varied by a multiple of the spatial period ( $\Lambda = 14.6 \mu\text{m}$ ). The cumulated fluence ranged from  $75.3 \text{ J cm}^{-2}$ – $113.0 \text{ J cm}^{-2}$ . The results are summarized in figure 8. The hatch distance was varied between  $292 \mu\text{m}$ – $438 \mu\text{m}$ .

The mean depth and the developed interfacial area ratio (ISO25178; Sdr) of a surface are coupled. The deeper the structures, the greater the developed surface area. The homogeneity of the microtextured surface can be characterized by the kurtosis factor (Pku). The kurtosis uses the fourth power of the root mean square deviation  $Rq$  to represent the dimensionless fourth power of the sampling length  $Z(x)$  and is given by equation (3)

$$\text{Pku} = \frac{1}{Rq^4} \left[ \frac{1}{lr} \int_0^{lr} Z^4(x) dx \right]. \quad (3)$$

An ideally sinusoidally developed surface has a kurtosis of 1.5. Since in this application the inhomogeneity occurs in the overlap region between two lines, a deviation in this region increases the kurtosis factor. To find the optimal process parameters, the highest Sdr factor as well as the Pku factor closest to 1.5 are desirable. In that way, the optimum for homogeneity was found using a hatch distance of  $365.5 \mu\text{m}$  and the corresponding topographical image is shown in figure 8(b).

Further work focused on identifying the variation of the DLIP period  $\Lambda$  across the scan field and optimizing the process in the presence of this error for 1064 nm. Figure 9 shows the scanfield analysis with respect to the spatial period variation starting from a target spatial period of  $15.0 \mu\text{m}$  in the center of the scan field (position 0,0). Compared to the simulated spatial period of  $15.4 \mu\text{m}$  is only a small deviation of 2.6%.

At the edges of the scan field, the DLIP spatial period increases to  $15.8 \mu\text{m}$ , which is a variation of 5.1%. A part of this effect is introduced by the increasing telecentricity error of the F-theta lens for deflection angles up to  $11.6^\circ$ . This leads to a variation of the angle between the interfering partial beams. In addition, the telecentricity error angle leads to a projection of the interference pattern and thus to a further increase in the space period as the pair of beams moves toward the edge of the scan field width.

But even with an ideally telecentric beam, spatial period variation can occur. Because there is a slightly different spatial period in front of, in, and behind the focal plane. Only in the case of an ideal, planar focal plane without image field curvature does this effect not occur over the entire scan field. Therefore, only without telecentric errors and a flat focal plane is there a constant spatial period over the scan field. For future applications, it would also be conceivable that F-theta optics are used, in which both effects compensate for each other.

In this work, the effect becomes significant with the number of periods in the DLIP pixel. At a hatch distance of  $360 \mu\text{m}$

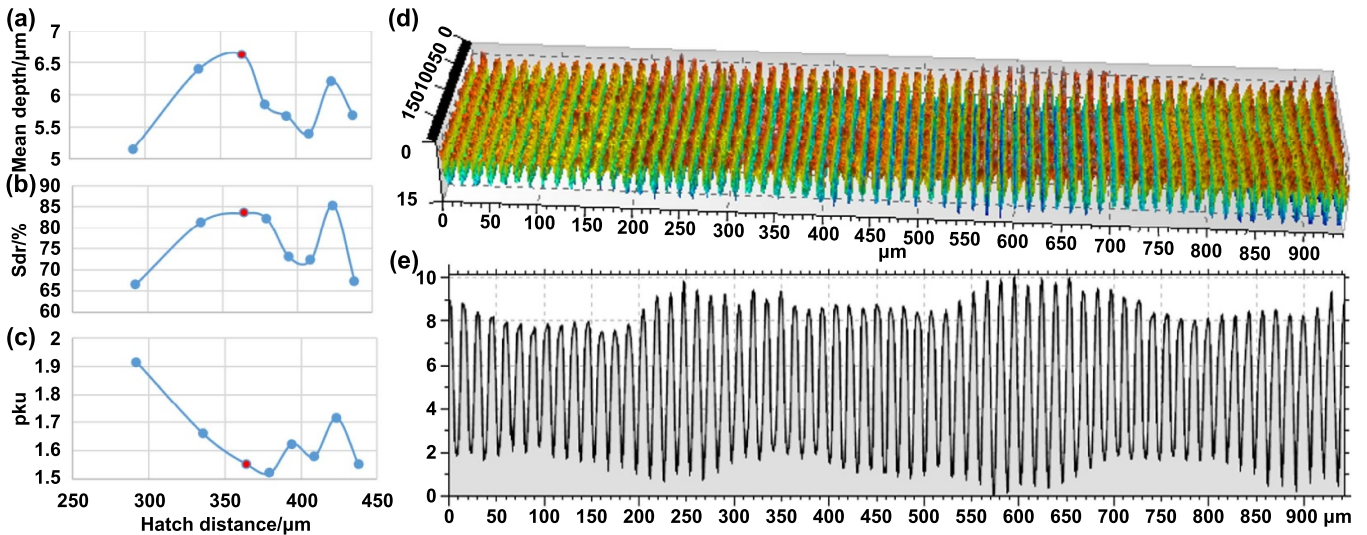


**Figure 8.** Results from the hatch distance optimization study. The optimum indicated by the red dot in (a)–(c) is 360 μm or 24 times the spatial period. The topography of the optimized surface texture is shown in (d) with the corresponding average profile (e).

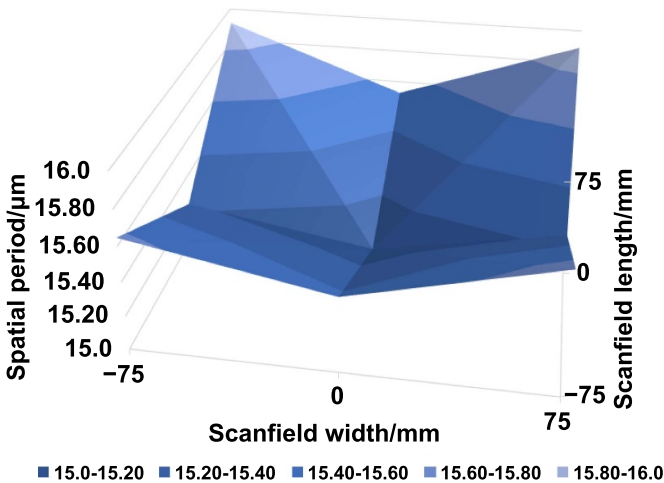


**Figure 9.** Analysis of the scan field showing the change in spatial period over the scan field, starting from a target period of 15.0 μm.

(or 24 times the spatial period), an offset of about 6 μm can be observed in the corners of the scan field at the overlapping maxima. Consequently, the ablations generated at the interference maxima no longer coincide in the overlap region between two subsequent lines, resulting in a periodic modulation of the depth. This error degrades the homogeneity and reduces the Sdr value of the surface. The observable microstructures show irregularities, especially at the edge of the scan field, so that the topographic properties such as Sdr (from 3.18% to 2.14%) as well as Pku (from 1.94 to 2.23) change negatively.

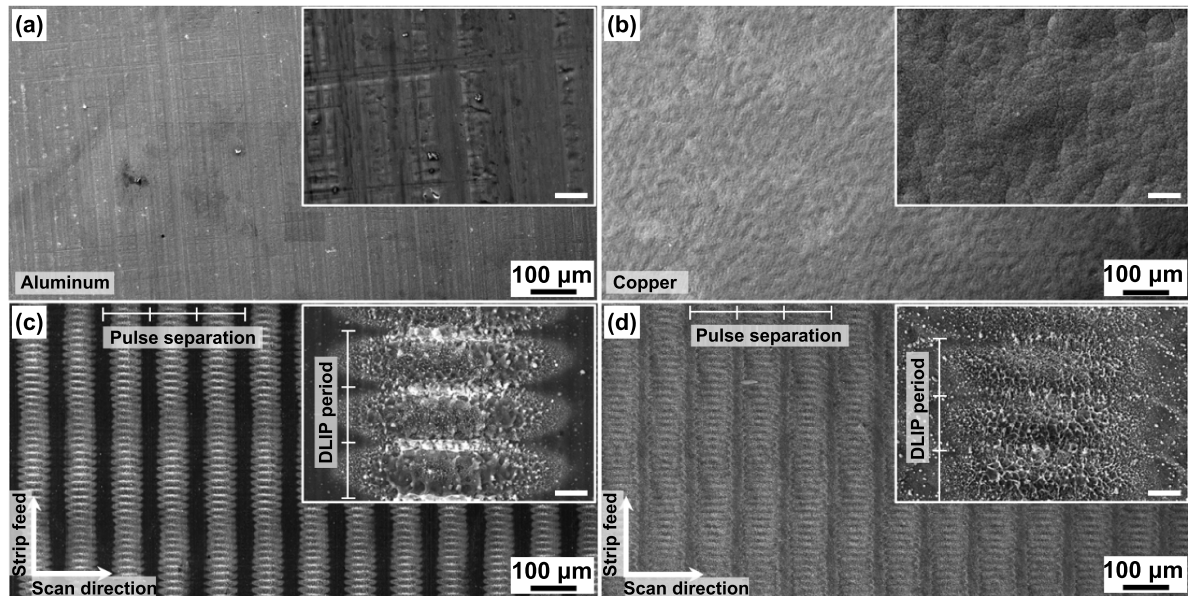
### 3.2. DLIP textured current collectors

Figure 10 shows scanning electron microscope images of DLIP-textured aluminum and copper foils at a wavelength

of 532 nm. Figures 10(a) and (b) show untreated foils with a roughness of  $S_a = 0.07 \mu\text{m}$  and  $S_z = 1.56 \mu\text{m}$  for aluminum and  $S_a = 0.14 \mu\text{m}$  and  $S_z = 1.36 \mu\text{m}$  for copper. Well-defined DLIP textures could be obtained on the foils with an optimized hatch distance of 243 μm. Figures 10(c) and (d) show textures obtained by ablation using 4 repetitions with a pulse spacing of 100 μm each. A cumulated laser fluence of  $5.1 \text{ J cm}^{-2}$ , average texture depths within the DLIP spots of 4 μm and 2 μm were achieved for aluminum and copper, respectively. Due to the small DLIP pulse width of about 50 μm, a clear separation between the individual DLIP spots is visible.

In addition, solidified melt can be seen in the magnification images for aluminum and copper at the positions of the interference maxima, indicating that melting still has a dominant influence on pattern formation for the thin foil material studied. This is in good agreement with another work by Bieda et al [33] on picosecond DLIP treatment of metals, where it was shown that laser processing with pulse durations above 5 ps can treat metals with the appropriate effects based on the classical theory of thermal conduction.

At high cumulative fluency values, this presents a challenge. The heat is not dissipated fast enough, which leads to undefined structures or even the cutting of the foil. In addition, thermal deformation of the film occurs, which can be observed in the R2R process by increased wrinkling. Therefore, the process was modified to reduce the heat input. Instead of increasing the overlap of the DLIP pixels (while reducing the processing speeds), the number of repetitions of each line was increased. This keeps the overlap constant at a low level between 16% and 33%. Thereby, the pulse generated heat has time to dissipate into the material, and the peak temperature decreases, reducing the deformation of the film. As a result, both the maximum speed of the scanner and the maximum power of the laser can be used.



**Figure 10.** SEM images of (a), (b) untreated and (c), (d) DLIP-textured films with a spatial period of  $15 \mu\text{m}$ . The pulse separation is shown in the figures and is  $100 \mu\text{m}$  for the textured foils. In addition, the DLIP period is highlighted in the insets, with the horizontal stripes marking the positions of the inference minima. Figures (a) and (c) show aluminum foil, while (b) and (d) show copper foil. The scale bars in the insets are  $10 \mu\text{m}$  in size.

To produce the aluminum foils for the subsequent electrode coating procedure, the laser power was reduced to  $59 \text{ W}$  to reduce foil deformation and to fabricate large sample areas ( $500 \text{ mm} \times 140 \text{ mm}$ ) using the ‘step-and-repeat’ method. The repetition frequency of the laser was set to  $100 \text{ kHz}$  at a pulse energy of  $0.59 \text{ mJ}$ . When the output power of the laser is changed, the position of the top-hat profile moves along the propagation axis and may no longer coincide precisely with the working position (as illustrated in figure 7). Before each experiment, the top-hat profile is verified using a beam profile camera at the working position. A mirror placed between the scanner and the camera reflects 99% of the intended power to a beam bump and transmits the smaller portion to the sensor. Then the first cylindrical telescope is adjusted to correct the divergence of the sub-beam and recover the optimal top-hat energy distribution at this power level.

The spacing between pulses was set at  $50 \mu\text{m}$  (overlap 16.7%), corresponding to a scanning speed of  $5000 \text{ mm s}^{-1}$ . The number of repetitions (called overscans) was increased from 1 to 10. The cumulative fluence was  $3.0 \text{ J cm}^{-2}$ . The best results were obtained with a hatch distance of  $390 \mu\text{m}$ . The homogeneity of the fabricated samples is a compromise of overlap and associated film deformation.

For the first copper samples, the laser power at  $1064 \text{ nm}$  had to be increased to  $64 \text{ W}$  (pulse energy of  $0.64 \text{ mJ}$ ) because copper reflects more of the incident IR radiation. Overlap was increased to 33% by reducing the processing speed to  $4000 \text{ mm s}^{-1}$ . The best results were obtained with a hatch distance of  $360 \mu\text{m}$ .

Color blackening increases with the number of scans (see figure 11), as deeper structures can be created by increasing the overscans. Increasing thermal deformation with increasing overscan also becomes more apparent.



**Figure 11.** Images of battery foils textured on the R2R machine depending on the number of scans. The single pulse fluence was kept constant at  $2.87 \text{ J cm}^{-2}$ . The overlap and hatch distance were kept constant at 20% and  $360 \mu\text{m}$ , respectively. Increasing the number of scans leads to deeper microstructures, but also to creases at the edges of the field. The textured area on each foil is  $500 \times 150 \text{ mm}$  and the scale bars in the figure correspond to  $120 \text{ mm}$ .

### 3.3. Technical limitations and opportunities for improvement

Due to their low thickness, the foils are sensitive to high energy impacts. At high power and with an increasing number of laser pulses per area (increased cumulated fluence), more deformation renders the process more difficult to control or the foils harder to use in later stages of the cell fabrication. A trade-off has to be made between processing speed and the achieved geometry. To increase the depth, it is more interesting to scan

**Table 2.** Process parameters of aluminum foil for cathodes.

Sample	Reprate (kHz)	Wavelength (nm)	Pulse width ( $\mu\text{m}$ )	Pulse sep. ( $\mu\text{m}$ )	Over-scan	Scan-speed ( $\text{mm s}^{-1}$ )	Hatch distance ( $\mu\text{m}$ )	Pulse energy (mJ)	Cum. fluence ( $\text{J cm}^{-2}$ )
C-DLIP-01	100	1064	50	50	1	5000	360	0.62	3.44
C-DLIP-02	100	1064	50	50	4	5000	360	0.62	13.78
C-DLIP-03	100	1064	50	50	7	5000	360	0.62	24.11
C-DLIP-04	100	1064	50	50	10	5000	360	0.62	34.44
C-DLIP-05	16	532	30	125	4	2000	243	0.31	4.08
C-DLIP-06	20	532	30	100	4	2000	243	0.31	5.10
C-DLIP-07	26.6	532	30	75	4	2000	243	0.31	6.80
C-DLIP-08	33.33	532	30	60	4	2000	243	0.31	8.50

**Table 3.** Process parameters of copper foil for anodes.

Sample	Reprate (kHz)	Wavelength (nm)	Pulse width ( $\mu\text{m}$ )	Pulse sep. ( $\mu\text{m}$ )	Over-scan	Scan-speed ( $\text{mm s}^{-1}$ )	Hatch distance ( $\mu\text{m}$ )	Pulse energy (mJ)	Cum. Fluence ( $\text{J cm}^{-2}$ )
A-DLIP-01	100	1064	50	40	1	4000	360	0.62	4.31
A-DLIP-02	100	1064	50	40	4	4000	360	0.62	17.22
A-DLIP-03	100	1064	50	40	7	4000	360	0.62	30.14
A-DLIP-04	100	1064	50	40	10	4000	360	0.62	43.06
A-DLIP-05	20	532	30	125	4	2000	243	0.31	4.08
A-DLIP-06	26.6	532	30	75	4	2000	243	0.31	6.80
A-DLIP-07	33.3	532	30	60	4	2000	243	0.31	8.50

the same line multiple times at lower energy with pauses to prevent heat accumulation. During the R2R process, this has been successfully achieved using an interleave scanning method. This method skips a few lines, leaving gaps that are filled later, letting the heat spread longer in the material and thus lowering the peak temperature.

For higher processing speed, a single scan with the highest and most homogeneous energy distribution (with top-hat beam forming) is used. To further increase the processing speed and reduce the dispersion in height and periodicity of the pattern, multiple solutions are considered. The first solution had already been implemented at the time of writing. It uses a complex lens that varies the focus across the scan field in order to compensate for the change in periodicity (presented in the previous section). This greatly increases the repeatability of the process with very homogeneous textures as well as a larger usable scan field. A second solution would be to use a more powerful laser source. It is then possible to use the higher order of the top hat while needing only a single scan to achieve the desired shape (depth). This increases the hatch distance and the band speed. Thirdly, a laser source capable of high pulse energy at a very high frequency (in the MHz range) can be used in combination with a polygon scanner that is very well suited for this application. The scanning speed will be greatly increased for the same geometry. Also, the off-time needed by a galvanometer scanner to jump back to the beginning of the line is entirely removed. Lastly, another improvement would be to further reduce the pulse duration. High power femto-second laser sources are becoming available and would limit the temperature and deformation of the material, reducing the trade-off criticality between speed and geometry.

In the R2R setup, the width of the textured band has already been optimized by rotating the scanner  $45^\circ$  relative to the

band direction. The diagonal of the scan field is scanned, which optimizes the use of both motorized mirrors. To further increase the band's width, we are again considering multiple solutions. The first is to increase the focal length of the focusing lens. This solution trades the minimal spatial period and the maximal focus for a larger scan field. The second is to divide the incoming beams with a beam splitter and make use of multiple scanners to process multiple parallel areas of the band at once. The system is flexible in that the spatial period can be adapted by changing the separation angle of the incident beams (equation (2)). It is directly dependent on the distance between the DOE and prism and the focal distance of the objective. However, the size of the scanner mirrors limits the partial beam separation. The spatial period of  $15 \mu\text{m}$  used in this work was dictated by the scanner aperture in combination with an objective whose scan field was large enough to texture an entire cell. Smaller spatial periods at a constant depth result in a larger developed area.

The effect of the geometric parameters (structure depth, spatial period) needs further investigation but could have a different effect on the cell's performance. Hypothetically, deeper structures with a spatial period closer to the mean diameter of the electrode particles could increase the anchoring effect. With a larger area of contact (Sdr), the resistance may decrease.

#### 3.4. Specific discharge capacity and peel-off test

The processing parameters of the textured current collectors are shown in tables 2 and 3. They were coated with composite electrode material and the electrodes were afterwards assembled in coin cells versus lithium (so-called half cells).

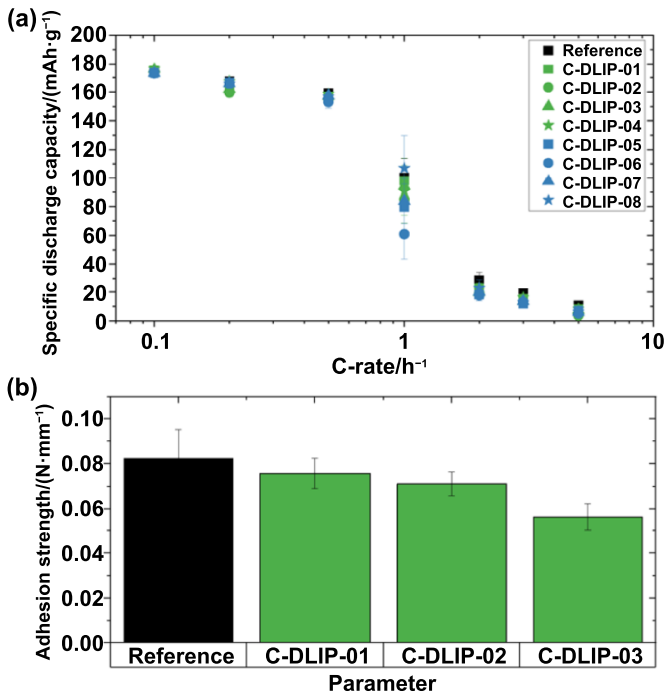


**Figure 12.** Displays for coin cell testing of cathode. (a) Electrochemical performance of coin cells containing NMC 622 electrodes with DLIP-textured current collectors; (b) the corresponding adhesion strengths of the NMC 622 electrodes.

The rate capacity analysis is shown in figure 12(a). At lower C-rates  $C/10$ ,  $C/5$  and  $C/2$ , no difference in discharge capacity was found for different cells. However, at 1 C, the cells containing NMC 622 cathodes with textured Al-foil with parameter C-DLIP-08 show higher discharge capacity in comparison to reference cells with standard unstructured aluminum foil. Besides, the cells containing textured Al-foil with parameter C-DLIP-01 exhibit almost the same capacity as the reference electrode, while cells with other types of textured current collectors display lower capacity at 1 C in comparison to reference cells. At 2C–5 C, cells with textured Al-foils show a  $5 \text{ mAh g}^{-1}$  lower discharge capacity. Therefore, the parameter C-DLIP-08 is the optimal parameter for the structuring of Al-foil for NMC 622 cathodes with a mass loading of  $25 \text{ mg cm}^{-2}$ .

Film adhesion strength was measured on uncalendered NMC 622 cathodes using the  $90^\circ$ -peel-off test, which is shown in figure 12(b). In comparison to cathodes with untextured current collectors, cathodes with textured current collectors exhibit lower adhesion strength. It is assumed that no anchoring effect exists for electrode materials on textured Al foil since the average diameter of NMC 622 particles is  $10\text{--}12 \text{ }\mu\text{m}$ , which is 1.5–2.5 times larger than the depth of DLIP-structures. Besides, the film adhesion deteriorates with increasing cumulated fluence. Thus, for the structuring of the Al current collector, a low laser fluence is beneficial to achieve higher adhesion strength.

The rate capability measurements and the peel adhesion strengths of the silicon/graphite composite electrodes for the different textured current collectors are shown in figure 13.

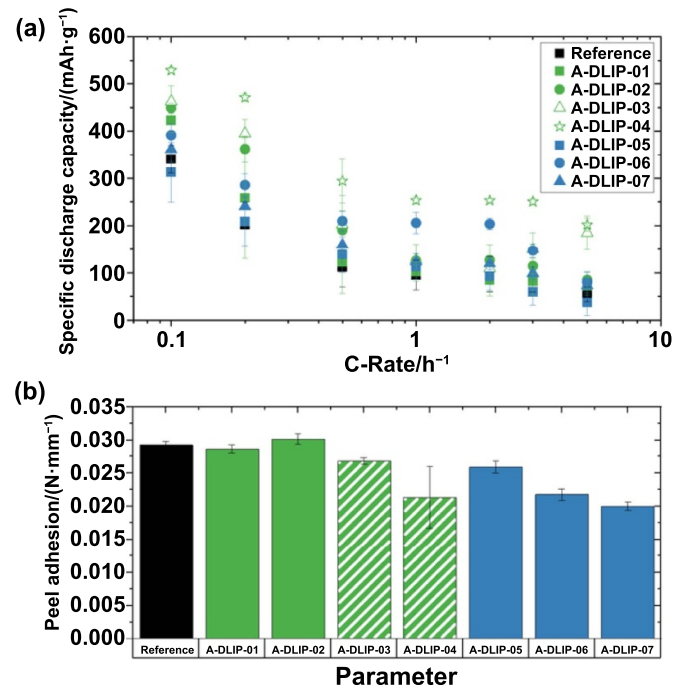


**Figure 13.** Displays for coin cell testing of anode. (a) Electrochemical performance of coin cells containing silicon/graphite composite electrodes with DLIP textured current collectors; (b) the corresponding adhesion strengths of the electrodes to the current collectors.

The electrodes with the textured current collectors A-DLIP-03 and A-DLIP-04 were not calendered since the current collector coiled and rendered the calendering step unfeasible. The electrodes therefore have a higher porosity (about 55%) compared to the calendered electrodes, which were compacted to reach a porosity of 40%. The specific discharge capacities shown in figure 13(a) reflect this, as the uncalendered electrodes show higher capacities compared to the calendered ones. Due to the coilage of the electrodes, the use of those parameters for the patterning of the current collectors is not recommended. In general, the specific discharge capacity decreases with increasing C-rates for all electrodes. Compared to the reference electrode, which was cast on an untextured current collector, an increase in specific discharge capacity can be observed at C-rates between  $C/10$  and 1 C for most electrodes with patterned current collectors. In this C-rate range, the most promising candidate is the textured current collector A-DLIP-04. At a C-rate of  $C/5$ , a specific discharge capacity of  $362 \text{ mAh g}^{-1}$  can be reached, whereas the reference electrode only reaches  $202 \text{ mAh g}^{-1}$ . At higher C-rates between 2C and 5 C, the highest specific discharge capacities can also be reached with the current collector, A-DLIP-04. Compared to the reference electrode, an increase of about 100% of specific discharge capacity can be observed at C-rates between  $C/2$  and 2C; for example, at 2C,  $97 \text{ mAh g}^{-1}$  can be reached for the reference electrode and  $204 \text{ mAh g}^{-1}$  for the electrode with current collector A-DLIP-04. Depending on the targeted usage of the electrodes and the expected C-rates, the DLIP pattern of A-DLIP-04 should be preferred.

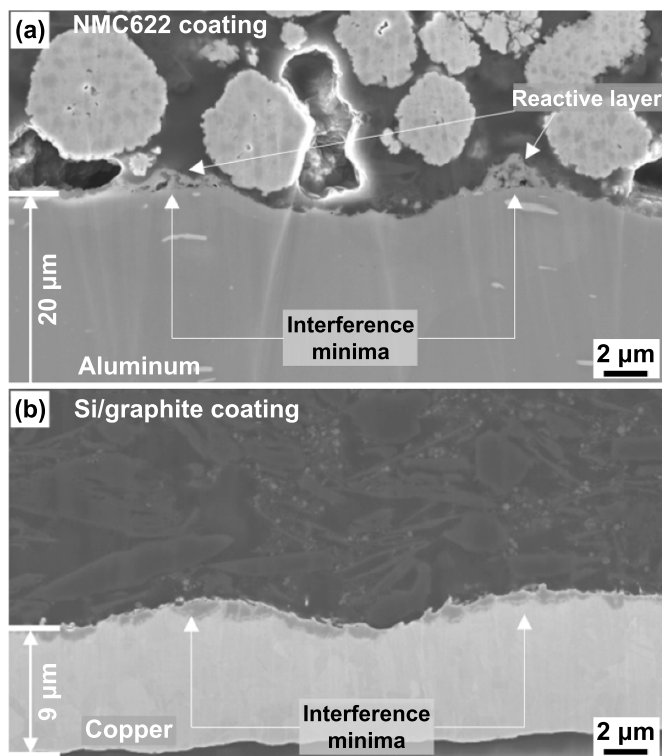


**Figure 14.** Focused ion beam polished cross-section of (a) coated Al foil and (b) coated Cu foil structured with  $15\ \mu\text{m}$  spatial period at  $5.1\ \text{J cm}^{-2}$ . At the Al foil the reactive layer is indicated at the interference minima positions.

When the peel adhesion measurements are compared, a slight increase in adhesion strength compared to the reference electrode can be observed for the electrode with a textured current collector with the parameter A-DLIP-02. All other textured current collectors decrease the peel adhesion strength compared to the reference electrode. Therefore, a clear correlation between the adhesion strength and the specific discharge capacities cannot be drawn so far. An increased cumulated laser fluence irradiating the current collector foil can lead to a decreased adhesion strength, which can be seen for the current collectors A-DLIP-05 to A-DLIP-07, where the accumulated fluence increased from  $4.08\ \text{J cm}^{-2}$ – $8.50\ \text{J cm}^{-2}$ . Since the calendaring step increases the film adhesion to the current collector and intrinsic film cohesion strength, the electrodes that were not calendared also reached significantly lower adhesion strengths ( $0.027 \pm 0.0005\ \text{N mm}^{-1}$  for A-DLIP-03 and  $0.020 \pm 0.0040\ \text{N mm}^{-1}$  for A-DLIP-04) compared to the reference electrode ( $0.029 \pm 0.0005\ \text{N mm}^{-1}$ ).

The adhesion bonding of coatings to textured foils was analyzed further using focused ion beam (FIB) cuts on the coated textured foils, as shown in figure 14. Figure 14(a) displays an NMC-coated Al foil, while figure 14(b) shows a Si/graphite Cu foil. In the FIB cuts, the interface area between the coating and the current collector foil was clearly visible. No delamination or cracking was found during inspection. However, on the aluminum foil, a porous material was observed on top of

the interference maxima. According to literature, this could be a relatively thick reactive layer resulting from the laser processing. Such a thick layer was not found on the Cu foil. As aluminum oxide is highly resistive, the formation of this oxide layer could explain the poor performance in cell testing of the cathodes. To prevent the formation of the reactive layer in future work, a shield gas such as nitrogen or argon gas should be applied.

#### 4. Conclusions

DLIP was used to texture current collector foils in a R2R process using a high-power picosecond pulsed laser system with 1064 nm and 532 nm wavelengths. With the generated line-shaped DLIP pixel with about  $15\ \mu\text{m}$  spatial period, copper and aluminum foils with  $9\ \mu\text{m}$  and  $20\ \mu\text{m}$  thickness, respectively, could be processed. High cumulated fluences of  $43.1\ \text{J cm}^{-2}$  on copper and  $34.4\ \text{J cm}^{-2}$  on aluminum led to a significant darkening of the foils and critical deformation. Smaller cumulated fluences of about  $6.1\ \text{J cm}^{-2}$  on copper and aluminum led to more flat structures with a depth of about  $1\ \mu\text{m}$ , but a significant decrease in the deformation and, in consequence, the possibility of being further coated with cathode and anode slurry. For the cathode material, an increased specific discharge capacity could be achieved at a C-rate of 1 C. For the anode material, improved rate capability at all C-rates between C/10 and 5 C was achieved. The rate capability was increased up to 100% compared to reference material. At C-rates between C/2 and 2 C, the specific discharge capacity was increased to about  $200\ \text{mAh g}^{-1}$ , while the reference electrodes showed a specific discharge capacity of about  $100\ \text{mAh g}^{-1}$ , showing the potential of the DLIP technology for cost-effective production of battery cells with increased specific capacities. With the setup, web speeds of up to  $1.3\ \text{m min}^{-1}$  and thus a structuring speed of  $0.20\ \text{m}^2\ \text{min}^{-1}$  could be achieved with a web width of 150 mm. As a result, this work presents the first-ever approach to large-area scanner-based DLIP texturing with high processing speeds and has the capability to be transferred to various industrial applications.

#### Acknowledgments

This research was funded by the German Federal Ministry of Education and Research (BMBF), project NextGen-3DBat, Grant Number 03XP0198F and by the Fraunhofer Cluster of Excellence Advanced Photon Sources (CAPS).

#### ORCID iDs

Christoph Zwahr <https://orcid.org/0000-0003-0575-4234>  
 Alexandra Meyer <https://orcid.org/0000-0001-7588-9746>  
 Wilhelm Pflöging <https://orcid.org/0000-0002-9221-9493>

## References

- [1] European Commission 2019 *Communication COM/2019/640: The European Green Deal* (Brussels: European Commission)
- [2] Pflöging W 2018 A review of laser electrode processing for development and manufacturing of lithium-ion batteries *Nanophotonics* **7** 549–73
- [3] Pflöging W and Pröll J 2014 A new approach for rapid electrolyte wetting in tape cast electrodes for lithium-ion batteries *J. Mater. Chem. A* **2** 14918–26
- [4] Haselrieder W, Westphal B, Bockholt H, Diener A, Höft S and Kwade A 2015 Measuring the coating adhesion strength of electrodes for lithium-ion batteries *Int. J. Adhes. Adhes.* **60** 1–8
- [5] Zheng H H, Zhang L, Liu G, Song X Y and Battaglia V S 2012 Correlation between electrode mechanics and long-term cycling performance for graphite anode in lithium ion cells *J. Power Sources* **217** 530–7
- [6] Chen L B, Xie X H, Xie J Y, Wang K and Yang J 2006 Binder effect on cycling performance of silicon/carbon composite anodes for lithium ion batteries *J. Appl. Electrochem.* **36** 1099–104
- [7] Romoli L, Lutey A H A and Lazzini G 2022 Laser texturing of Li-ion battery electrode current collectors for improved active layer interface adhesion *CIRP Ann.* **71** 481–4
- [8] Zheng Y, An Z, Smyrek P, Seifert H J, Kunze T, Lang V, Lasagni A F and Pflöging W 2016 Direct laser interference patterning and ultrafast laser-induced micro/nano structuring of current collectors for lithium-ion batteries *Proc. SPIE* **9736** 97361B
- [9] Chen J Q, Wang X G, Gao H T, Yan S, Chen S D, Liu X H and Hu X L 2021 Rolled electrode deposited copper foil with modified surface morphology as anode current collector for high performance lithium-ion batteries *Surf. Coat. Technol.* **410** 126881
- [10] Scholz C, Gebhardt M and Clair M 2021 Roll-to-roll laser processing of flexible devices *Lasers in Manufacturing Conf. 2021 (Munich, 21–24 June 2021)* vol 14 pp 16–21 (available at: [https://wlt.de/sites/default/files/2021-10/ablation\\_drilling\\_cutting/Contribution\\_244\\_final.pdf](https://wlt.de/sites/default/files/2021-10/ablation_drilling_cutting/Contribution_244_final.pdf))
- [11] Mincuzzi G, Bourterreau A, Sikora A, Faucon M and Kling R 2022 Pushing laser nano-structuring through mass production *Proc. SPIE* **11989** 119890
- [12] Lasagni A and Mücklich F 2009 FEM simulation of periodical local heating caused by laser interference metallurgy *J. Mater. Process. Technol.* **209** 202–9
- [13] Voisiat B, Gedvilas M, Indrišiūnas S and Račiukaitis G 2011 Picosecond-laser 4-beam-interference ablation as a flexible tool for thin film microstructuring *Phys. Proc.* **12** 116–24
- [14] Hans M, Gachot C, Müller F and Mücklich F 2009 Direct laser interference structuring as a tool to gradually tune the wetting response of titanium and polyimide surfaces *Adv. Eng. Mater.* **11** 795–800
- [15] Lang V, Roch T and Lasagni A F 2016 World record in high speed laser surface microstructuring of polymer and steel using direct laser interference patterning *Proc. SPIE* **9736** 97360Z
- [16] Milles S, Voisiat B, Nitschke M and Lasagni A F 2019 Influence of roughness achieved by periodic structures on the wettability of aluminum using direct laser writing and direct laser interference patterning technology *J. Mater. Process. Technol.* **270** 142–51
- [17] Finger J, Kalupka C and Reininghaus M 2015 High power ultra-short pulse laser ablation of IN718 using high repetition rates *J. Mater. Process. Technol.* **226** 221–7
- [18] El-Khoury M, Voisiat B, Kunze T and Lasagni A F 2022 Utilizing a diffractive focus beam shaper to enhance pattern uniformity and process throughput during direct laser interference patterning *Materials* **15** 591
- [19] Kunze T, Zwahr C, Krupop B, Alamri S, Rößler F and Lasagni A F 2017 Development of a scanner-based direct laser interference patterning optical head: new surface structuring opportunities *Proc. SPIE* **10092** 1009214
- [20] Madelung A, Alamri S, Steege T, Krupop B, Lasagni A F and Kunze T 2021 Scanner-based direct laser interference patterning on stainless steel *Adv. Eng. Mater.* **23** 2001414
- [21] Račiukaitis G 2011 Laser processing by using diffractive optical laser beam shaping technique *J. Laser Micro Nanoeng.* **6** 37–43
- [22] Basler C, Brandenburg A, Michalik K and Mory D 2019 Comparison of laser pulse duration for the spatially resolved measurement of coating thickness with laser-induced breakdown spectroscopy *Sensors* **19** 4133
- [23] Wiegmann M, Dreisewerd K and Soltwisch J 2016 Influence of the laser spot size, focal beam profile, and tissue type on the lipid signals obtained by MALDI-MS imaging in oversampling mode *J. Am. Soc. Mass Spectrom.* **27** 1952–64
- [24] Rung S 2013 Laserscribing of thin films using top-hat laser beam profiles *J. Laser Micro Nanoeng.* **8** 309–14
- [25] Bischoff C, Jäger E, Umhofer U, Lasagni A F and Völklein F 2020 Homogeneous intensity within the Rayleigh length and enhanced depth of focus for Gaussian beams *J. Laser Micro Nanoeng.* **15** 178–85
- [26] Bischoff C, Rädcl U, Umhofer U, Jäger E and Lasagni A F 2022 Integration of diffractive optics for top-hat generation and enhanced depth of focus *J. Laser Micro Nanoeng.* **17** 69–80
- [27] Veldkamp W B and Kastner C J 1982 Beam profile shaping for laser radars that use detector arrays *Appl. Opt.* **21** 345–56
- [28] Veldkamp W B 1982 Laser beam profile shaping with interlaced binary diffraction gratings *Appl. Opt.* **21** 3209–12
- [29] Gur I and Mendlovic D 1998 Diffraction limited domain flat-top generator *Opt. Commun.* **145** 237–48
- [30] Zhu P H, Seifert H J and Pflöging W 2019 The ultrafast laser ablation of  $\text{Li}(\text{Ni}_{0.6}\text{Mn}_{0.2}\text{Co}_{0.2})\text{O}_2$  electrodes with high mass loading *Appl. Sci.* **9** 4067
- [31] Meyer A, Ball F and Pflöging W 2021 The effect of silicon grade and electrode architecture on the performance of advanced anodes for next generation lithium-ion cells *Nanomaterials* **11** 3448
- [32] Zhu P, Han J and Pflöging W 2021 Characterization and laser structuring of aqueous processed  $\text{Li}(\text{Ni}_{0.6}\text{Mn}_{0.2}\text{Co}_{0.2})\text{O}_2$  thick-film cathodes for lithium-ion batteries *Nanomaterials* **11** 1840
- [33] Bieda M, Siebold M and Lasagni A F 2016 Fabrication of sub-micron surface structures on copper, stainless steel and titanium using picosecond laser interference patterning *Appl. Surf. Sci.* **387** 175–82